









Polar discontinuity governs surface segregation and interface termination: A case study of $\text{LaInO}_3/\text{BaSnO}_3$

Martina Zupancic ^{1,*}, Wahib Aggoune,² Alexandre Gloter,³ Georg Hoffmann ⁴, Franz-Philipp Schmidt ⁵,
Zbigniew Galazka ¹, Daniel Pfützenreuter,¹ Aysha A. Riaz,⁶ Christoph Schlueter,⁷ Houari Amari,¹ Anna Regoutz,⁶
Jutta Schwarzkopf ¹, Thomas Lunkenbein,⁵ Oliver Bierwagen ⁴, Claudia Draxl ² and Martin Albrecht ¹

¹Leibniz-Institut für Kristallzüchtung, Max-Born-Straße 2, 12489 Berlin, Germany

²Institut für Physik and IRIS Adlershof, Humboldt-Universität zu Berlin, Zum Großen Windkanal 2, 12489 Berlin, Germany

³Université Paris-Saclay, CNRS Laboratoire de Physique des Solides, Orsay 91405, France

⁴Paul-Drude-Institut für Festkörperelektronik, Leibniz-Institut im Forschungsverbund Berlin e.V.,
Hausvogteiplatz 5–7, 10117 Berlin, Germany

⁵Fritz-Haber-Institut der Max-Planck-Gesellschaft, Faradayweg 4–6, 14195 Berlin, Germany

⁶Department of Chemistry, University College London, 20 Gordon Street, London WC1H 0AJ, United Kingdom

⁷Deutsches Elektronen-Synchrotron DESY, Notkestraße 85, 22607 Hamburg, Germany



(Received 11 December 2023; revised 14 February 2024; accepted 26 February 2024; published 29 March 2024)

We combine (scanning) transmission electron microscopy, electron energy loss spectroscopy (EELS), and x-ray photoelectron spectroscopy (XPS) with density functional theory (DFT) to investigate the complex interplay of surface energetics and polar discontinuity compensation in the interface formation of (001) $\text{LaInO}_3/\text{BaSnO}_3$ -based heterostructures. We present evidence from both experiment and theory that the BaSnO_3 surface with BaO termination is energetically favored over a wide range of chemical potentials. However, overgrowth of the nonpolar BaO -terminated surface with LaInO_3 results in a SnO_2 -terminated interface. EELS and XPS show that this interfacial termination exchange is mediated by Ba segregation to the growth surface. Our DFT calculations show that the efficient compensation of the polar discontinuity, attributed to polar distortions within BaSnO_3 at the SnO_2 -terminated interface, serves as the driving force behind the observed Ba segregation. This intricate interplay underscores the importance of polar discontinuity compensation as a pivotal factor influencing interface formation in perovskite systems.

DOI: [10.1103/PhysRevMaterials.8.034602](https://doi.org/10.1103/PhysRevMaterials.8.034602)

I. INTRODUCTION

Interface polar discontinuities provide a unique means to control charge states at interfaces and generate two-dimensional (2D) electron systems. Early examples of such heterojunctions include the interface between closely lattice-matched GaAs and Ge [1,2]. Another well-documented case is the interface between AlN and GaN , where a discontinuity in spontaneous polarization leads to the formation of 2D electron gas (2DEG) or hole gas [3]. Polar-nonpolar interfaces between ABO_3 perovskites offer opportunities for tuning interface states due to the presence of mixed-valence states [4,5]. This 2DEG has the potential to undergo electronic phase transitions leading to superconducting or magnetic properties, paving the way for innovative device applications [6,7].

The widely accepted model for 2DEG formation is based on the concept of charge transfer between the layers terminating the polar-nonpolar interface. In the classic example of the $\text{LaAlO}_3/\text{SrTiO}_3$ polar-nonpolar interface, the LaO^+ layer on TiO_2^0 contributes 0.5 electrons, thereby promoting the formation of a 2DEG [4,8]. Similarly, an AlO_2^- layer on SrO^0 donates 0.5 holes, resulting in a 2D hole gas. Achieving precise atomic-level control over the surface of nonpolar

perovskites in epitaxial growth is therefore a key factor in realizing one or the other [9]. In general, the (001) surface of ABO_3 perovskites represents the most energetically stable facet, with two possible terminations, AO and BO_2 [10]. If we consider ionic charges, these terminations remain neutrally charged along $\langle 100 \rangle$ directions as observed in perfect cubic perovskites (space group $Pm\bar{3}m$), while in the case of orthorhombic symmetry (space group $Pbnm$), the terminations can be either positively or negatively charged along $[100]_{\text{pc}}$, $[010]_{\text{pc}}$, and $[001]_{\text{pc}}$ directions. In heterostructure growth, the surface termination of the nonpolar neutrally charged layer is commonly assumed to control the interface behavior, although cation mixing may influence interface formation [11].

In this paper, we elucidate the interplay between polar discontinuity compensation and surface segregation, which fundamentally affects interface termination. We focus on the interface between the wide-band-gap cubic semiconductor BaSnO_3 and orthorhombic LaInO_3 [12–15]. The recent surge of interest in 2DEG at the $\text{LaInO}_3/\text{BaSnO}_3$ interface is due to the remarkable electron mobility of BaSnO_3 at room temperature, which exceeds that of other perovskite oxides [12]. We use a combination of analytical scanning transmission electron microscopy (STEM)-based techniques, x-ray photoelectron spectroscopy (XPS), and density functional theory (DFT) calculations to solve this puzzle.

*martin.albrecht@ikz-berlin.de

Our transmission electron microscopy (TEM) experiments on the pristine surface of BaSnO₃ bulk crystals and on the surface of BaSnO₃ thin films, corroborated by DFT findings, consistently indicate the predominance of BaO as the surface termination for BaSnO₃ over a wide range of chemical potentials. However, at the interface between BaSnO₃ and LaInO₃, a SnO₂ termination is observed by electron energy loss spectroscopy (EELS). This finding is consistent with the presence of a 2DEG and agrees with our DFT calculations, which identify this interface as the energetically most favorable. Furthermore, STEM-EELS and XPS provide evidence for the presence of BaO on the surface of thin LaInO₃ films grown on BaSnO₃, a strong indication of Ba surface segregation. According to our DFT calculations, it is the compensation of the interfacial polar discontinuity that drives the segregation of Ba. This compensation process is facilitated by the gradual reduction of the octahedral tilt as we move from orthorhombic LaInO₃ to cubic BaSnO₃, along with the polar and nonpolar distortions at the interface. Remarkably, our results highlight the efficiency of the *n*-type SnO₂ interface in compensating for this discontinuity. In the context of perovskites, it is thus important to recognize that, in addition to the well-known factors of surface energy, solubility, and strain that drive segregation in classical group IV and III–V semiconductor alloys, the response of the system to compensate for the polar-nonpolar discontinuity serves as an additional driving force for segregation [16–19]. This response can ultimately determine the termination of the interface.

A. Crystallography of BaSnO₃ and LaInO₃

BaSnO₃ crystallizes in the perfect cubic perovskite structure, which can be described by the space group $Pm\bar{3}m$ and can be considered a nonpolar material. The lattice constant of bulk BaSnO₃ of 4.119 Å, obtained with the PBEsol functional, is in good agreement with the experimental value of 4.116 Å reported by Maekawa *et al.* [14,20]. Here, SnO₆ octahedra have high symmetry without tilting. Considering the ionic charges of Ba (+2), Sn (+4), and O (−2), BaSnO₃ is composed of neutral BaO⁰ and SnO₂⁰ layers that alternate along the $\langle 100 \rangle$ directions [14].

LaInO₃ is an orthorhombic perovskite with a pseudocubic lattice constant of 4.116 Å which perfectly matches that of BaSnO₃ [14,21,22]. The crystal symmetry of LaInO₃ with the lattice parameters $a = 5.70$ Å, $b = 5.94$ Å, and $c = 8.21$ Å belongs to space group $Pbnm$ which is also centrosymmetric [14]. LaInO₃ is composed of La (+3), In (+3), and O (−2), while charged polar planes of LaO⁺ and InO₂[−] alternate along the $[100]_{pc}$, $[010]_{pc}$, and $[001]_{pc}$ directions. However, due to centrosymmetry, the dipoles cancel each other out in the bulk LaInO₃. The oxygen octahedral tilt can be described by $a^-a^-c^+$ in the Glazer notation, while the orthorhombic and pseudocubic relationship of the LaInO₃ unit cell is described by Zupancic *et al.* [23,24].

II. EXPERIMENTAL AND CALCULATION DETAILS

A. Growth of BaSnO₃ single crystals and LaInO₃/BaSnO₃ heterostructures

Bulk BaSnO₃ single crystals were grown from the melt as described by Galazka *et al.* [25]. BaSnO₃ (001) surfaces of

single crystals were oriented by x-ray diffraction and were prepared by mechanical polishing using diamond lapping foils. This was followed by chemomechanical polishing, using a 0.02 μm SiO₂ suspension. After polishing, the BaSnO₃ single crystals were annealed at 1100 °C for 1 h in an oxygen atmosphere at a heating rate of 15 °C/min.

LaInO₃/BaSnO₃ heterostructures were grown on DyScO₃ substrates by plasma-assisted molecular beam epitaxy (MBE). The DyScO₃ substrate was preannealed in a tube furnace at 1050 °C for 6 h in an oxygen atmosphere to create a ScO₂-terminated surface [26]. The BaSnO₃ film was grown at a substrate temperature of 835 °C, measured with a pyrometer, and using a mixture of Sn and SnO₂ as the SnO source [27]. The Ba and SnO beam equivalent pressures were 9.12×10^{-8} and 9.14×10^{-8} mbar, respectively. The oxygen flux was set to 0.05 sccm, and the plasma power was set to 200 W. To keep the plasma ignited, 0.2 sccm of Ar was added to the gas flow. The resulting BaSnO₃ growth rate of 1.85 nm/min was measured by laser reflectometry. After deposition of the BaSnO₃ layer, the LaInO₃ layer was deposited on a BaSnO₃ film at the temperature of 925 °C (also measured with a pyrometer). The La and In beam equivalent pressures were 4.50×10^{-8} and 6.19×10^{-8} mbar, respectively. The oxygen flux was set to 0.06 sccm at a plasma power of 200 W. The resulting LaInO₃ growth rate was ~ 1.1 nm/min. More details on the LaInO₃ growth are given in Ref. [28].

LaInO₃/BaSnO₃ heterostructures grown by pulsed laser deposition (PLD) on (001) SrTiO₃ substrates were grown at 750 °C and 100 mTorr of oxygen pressure. Prior to BaSnO₃ film growth, the SrTiO₃ substrate surface was etched in a buffered HF and annealed at 1100 °C in a pure oxygen gas flow for 1 h. A KrF excimer laser with an energy fluence in the range of 1.2–1.5 J/cm² was used for the PLD growth, while PLD targets were provided by Toshiba Manufacturing Co. in Japan.

B. TEM sample preparation and analysis

Cross-sectional TEM samples were prepared by the sandwich technique, where two film sides of the heterostructure are bonded together with epoxy and glued onto a molybdenum support holder. The samples were further polished along the $\langle 100 \rangle$ and $[110]$ lattice directions of the BaSnO₃ using a tripod. Following mechanical polishing, the subsequent step involved chemomechanical polishing utilizing a 0.02 μm SiO₂ suspension. Further thinning of the samples was performed by Ar⁺ ion milling at liquid nitrogen temperature and using accelerating voltages from 3.7 to 0.2 kV using the Gatan precision ion-polishing system. Both BaSnO₃ single crystals and BaSnO₃-based heterostructures were analyzed by high-resolution transmission electron microscopy (HRTEM) using an aberration-corrected FEI Titan 80–300 operated at 300 kV. The spherical aberration (C_s) is set to a slightly negative value. Due to the negligible difference in the atomic numbers of Ba and La as well as Sn and In of only 1, it is not possible to distinguish them by using high-angle annular dark-field (HAADF) imaging in STEM. Therefore, our analysis is based on STEM-EELS measurements. STEM and EELS analysis of an MBE grown sample was performed using a C_s -corrected Nion Ultra STEM microscope at an

operating voltage of 100 kV. The EELS spectra obtained by the Nion Ultra STEM microscope were acquired using a modified Gatan spectrometer and a MerlinEELS detector from Quantum Detectors. The EELS intensities of the Ba $M_{4,5}$, La $M_{4,5}$, Sn $M_{4,5}$, and In $M_{4,5}$ edges are used for the interface termination analysis. The EELS analysis of the MBE sample was carried out using convergence and collection semiangles set to 30 and 50 mrad, respectively, with an energy dispersion of 0.69 eV/channel. A beam current of ~ 50 pA was used. In addition, STEM and EELS analysis of the PLD grown sample was performed using a probe and image-corrected JEOL JEM-Atomic Resolution Microscope 200F operated at 200 kV and equipped with a Gatan GIF Quantum spectrometer. The EELS investigation of the PLD sample was conducted using convergence and collection semiangles set to 15.6 and 20.1 mrad, respectively, and a beam current of 30 pA. The energy dispersion was 0.25 eV/channel, while dual EELS was used for the energy drift correction. Soft XPS (SXPS) and hard XPS (HAXPES) were used to investigate a series of MBE grown heterostructures with various LaInO_3 overlayer thicknesses ranging from 4 to 8 nm as well as bulk layers of BaSnO_3 and LaInO_3 . Laboratory-based SXPS was performed on a Thermo Scientific K-Alpha spectrometer with a monochromated microfocused Al $K\alpha$ x-ray source ($h\nu = 1486.7$ eV) and a spot size of 400 μm . The base pressure of the instrument was 2×10^{-9} mbar, and the x-ray source was operated at 6 mA emission current and 12 kV anode bias. A pass energy of 20 eV was used to collect all core level spectra, and a flood gun was used to minimize sample charging. All SXPS data were aligned to the adventitious C 1s signal at 284.8 eV. HAXPES data were collected at beamline P22 at PETRAIII, German Electron Synchrotron DESY in Hamburg, Germany [29]. Two photon energies were used to provide varying probing depth, including 3.4 keV [selected using Si (111) and (220)] and 6 keV [selected using Si (311)]. All measurements were conducted in grazing incidence geometry (5°). A Phoibos 225HV analyzer (SPECS, Berlin, Germany) was used with the small area lens mode and a slit size of 3 mm. Spectra were collected using a pass energy of 30 eV. All HAXPES data were aligned to the respective Fermi energy position of a gold reference.

C. First-principles calculations

The calculations are performed using DFT [30,31], within the generalized gradient approximation for the exchange-correlation functional in the PBEsol parameterization [32]. All calculations are performed using FHI-aims [33], an all-electron full-potential package. The code is based on numerical atom-centered orbitals. For all atomic species we use *tight* setting with a *tier 2* basis set for oxygen (O), *tier 1 + fg* for barium (Ba), *tier 1 + gpdf* for tin (Sn), *tier 1 + hfdg* for lanthanum (La), and *tier 1 + gpflh* for indium (In). Cleavage and surface energies of BaSnO_3 are calculated using the symmetric slab model. A thickness of 6 unit cells is found to be good enough to converge the surface energy [34]. For such slabs, we include a vacuum of 150 \AA and apply a dipole correction in the nonperiodic out-of-plane [001] direction to avoid unphysical interactions between neighboring replicas. The in-plane lattice parameters are fixed to those

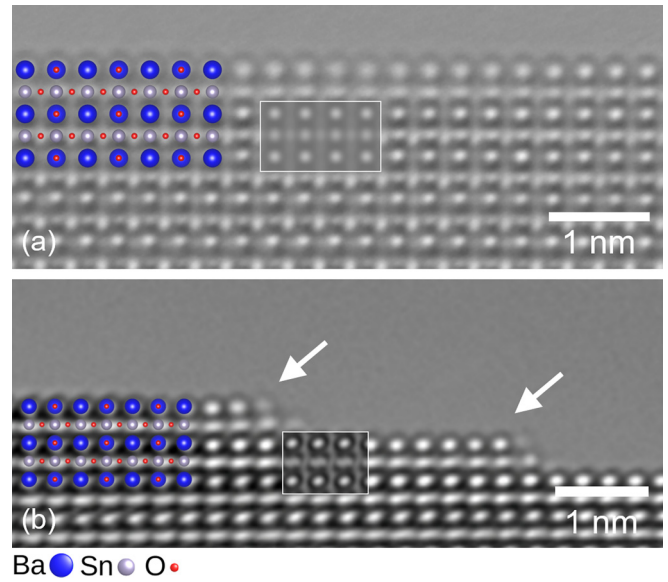


FIG. 1. (a) BaSnO_3 (001) single crystal and (b) thin film surfaces viewed along the [110] direction under TEM high-vacuum conditions. HRTEM simulations are shown as white-framed insets, while white arrows shown in (b) are pointing to the 1-unit-cell-high surface steps.

of the optimized bulk BaSnO_3 , and the internal coordinates are optimized until the residual forces on each atom are <0.001 eV/ \AA . Brillouin zone (BZ) sampling is performed with an $8 \times 8 \times 1$ k grid for the (001) BaSnO_3 surface slab. For bulk BaSnO_3 , an $8 \times 8 \times 8$ k -point mesh is adopted. For periodic $\text{LaInO}_3/\text{BaSnO}_3$ superlattices, the sampling of the BZ is performed with a $6 \times 6 \times 1$ k grid. For the heterostructures, the in-plane lattice parameters are fixed to those of bulk BaSnO_3 . In this case, the out-of-plane lattice constant and the internal coordinates are optimized until the residual forces on each atom are <0.001 eV/ \AA . The atomic structures are visualized using VESTA software [35].

III. EXPERIMENTAL RESULTS

A. Atomic structure of BaSnO_3 (001) surface

Figure 1(a) shows an HRTEM image of the (001) surface of a BaSnO_3 single crystal along [110]. The corresponding image simulation, highlighted by a white frame, shows that the surface is BaO terminated. The image was taken for a negative C_s of -12 μm and defocus (Δf) of 6 nm. From image simulations we find the best agreement of the image pattern for a sample thickness (t) of 1.2 nm. An atomic model of BaSnO_3 is superimposed on the high-resolution image pattern. The blue, gray, and red atomic columns in the atomic model correspond to Ba, Sn, and O, respectively. Figure 1(b) shows the surface of a heteroepitaxial PLD-grown BaSnO_3 film on a SrTiO_3 substrate. The BaSnO_3 surface contains two surface steps, each 1 unit cell high and always terminated by a BaO layer. For the given imaging conditions ($C_s = -12$ μm , $\Delta f = 9$ nm and a small astigmatism value ($A1$) of 2 nm at -70°), the thickness of the sample in the analyzed area is 2.9 nm.

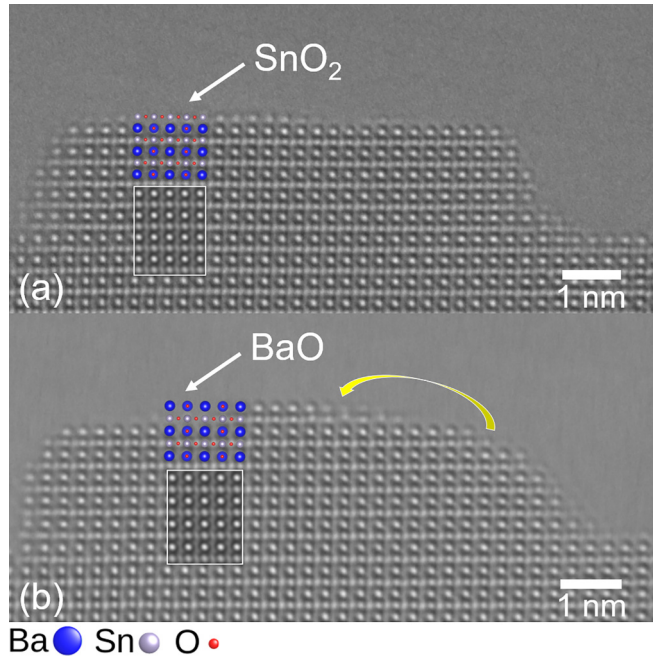


FIG. 2. BaSnO₃ single crystal (001) surface seen along [110] projection under high-vacuum conditions and electron beam (a) before and (b) after 15 s. HRTEM simulations are shown as white-framed insets, while yellow arrow in (b) shows the direction of the atomic reconstruction of the surface exposed to the electron beam.

Figure 2 shows experimental HRTEM images of the (001) surface of a BaSnO₃ single crystal along the [110] projection. The surface is rough due to the TEM sample preparation. From the image simulations ($C_s = -12 \mu\text{m}$, $\Delta f = 8 \text{ nm}$, $A1 = 1 \text{ nm}$ at 50° , $t = 1.7 \text{ nm}$) that are shown as an inset, we can assign Sn and Ba atoms. A small part of the (001) surface is covered with an SnO₂ layer. During the TEM observation, i.e., with electron irradiation at an accelerating voltage of 300 kV (beam current of 0.15 nA) and time (15 s), the Ba atoms rearrange from the side facets toward the (001) facet, as indicated by the yellow arrow, covering the small SnO₂-terminated region and forming a BaO-terminated surface [Fig. 2(b)]. The yellow arrow here represents the direction of atomic displacement at the BaSnO₃ surface during the observation. Note that all surfaces depicted in Figs. 1 and 2 do not represent the as-grown surfaces of BaSnO₃. Instead, they are the outcome of Ar⁺ ion beam thinning during TEM sample preparation.

B. Atomic structure of the LaInO₃/BaSnO₃ interface

A high-resolution dark-field STEM image of the LaInO₃/BaSnO₃ interface of an MBE grown sample is shown in Fig. 3(a) and covers the lateral field of view of $\sim 9 \text{ nm}$ from which the EELS profiles were extracted. Figure 3(b) shows the magnified part of the heterostructure marked by the yellow box in Fig. 3(a). The atomic model superimposed on the high-resolution dark-field STEM image in Fig. 3(b) shows LaInO₃ along the [100] pseudocubic direction, while BaSnO₃ is seen along the [100] crystallographic direction. The surface normal corresponds to the [001] pseudocubic

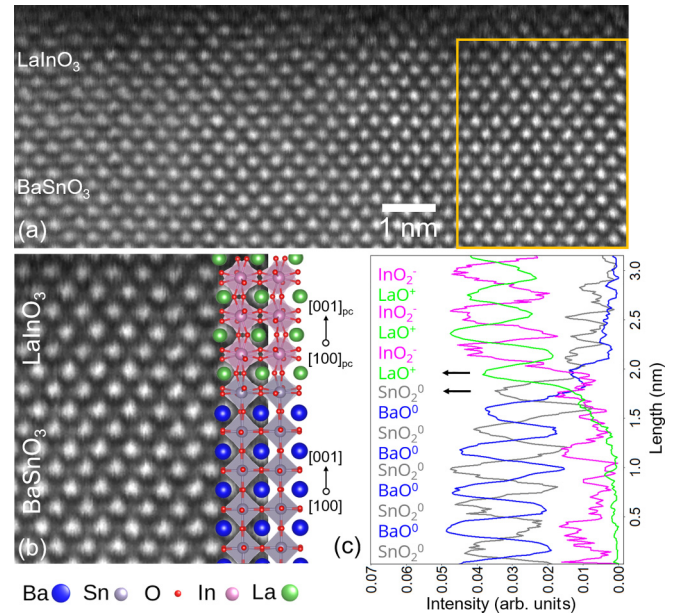


FIG. 3. (a) High-resolution dark-field STEM image of the region where the EELS intensities are extracted. (b) Magnified dark-field STEM image of the region inside the yellow box shown in (a) with overlaid supercell built by DFT. (c) Laterally averaged EELS intensities of the Ba, Sn, La, and In $M_{4,5}$ edges showing the LaO/SnO₂ plane termination at the LaInO₃/BaSnO₃ interface shown in (a).

direction of LaInO₃. Figure 3(c) shows laterally integrated EELS intensities of Ba, Sn, La, and In across the interface. The extracted EELS intensities clearly show the LaO/SnO₂ or n -type interface. More details on termination analysis are given in the Supplemental Material [34].

To gain insight into the mechanism promoting the SnO₂ termination of the interface and to study possible segregation or intermixing mechanisms, we performed similar EELS analysis of the MBE-grown sample with a 4-nm-thick LaInO₃ layer. To measure the surface composition by EELS, we protect the growth surface with an *in situ* deposited amorphous SiO₂ layer. This prevents cracking of the epoxy (which covers the surface of a cross-sectional TEM sample) by the electron beam during EELS analysis. The high-resolution dark-field STEM image in Fig. 4(a) shows the LaInO₃/BaSnO₃ heterostructure with eight boxes indicated, which are used for the EELS analysis. We integrate over 1×12 unit cells to improve the signal, as we need to reduce the beam current to avoid radiolysis and amorphization of the sample during the measurement. In regions 1 and 2, the Ba $M_{4,5}$ signal extracted in Fig. 4(b) is strong, then gradually decreases in region 3 and disappears completely within regions 4–6, i.e., in the LaInO₃ film. At the LaInO₃ surface (box 7), the Ba $M_{4,5}$ signal increases slightly and disappears in the last region (box 8). Within regions 1 and 2, no La $M_{4,5}$ signal is visible, indicating that these regions represent the BaSnO₃ layer. In regions 3–5, the La $M_{4,5}$ signal remains constant, while toward the surface, it decreases (box 6) and finally disappears (boxes 7 and 8). The increased Ba signal at the LaInO₃ surface clearly suggests the presence of Ba. The Ba- and La-edge intensities in the EELS spectra are only a qualitative measure for the

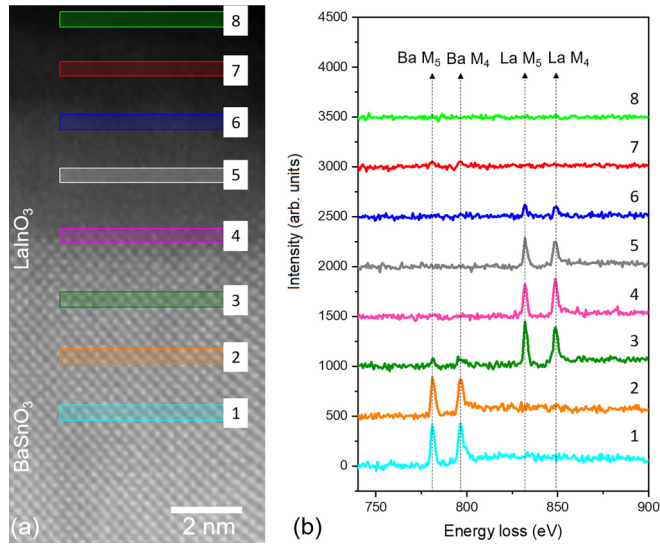


FIG. 4. (a) High-resolution dark-field STEM image of the $\text{LaInO}_3/\text{BaSnO}_3$ heterostructure grown by MBE showing the area used for the EELS analysis. (b) EELS spectra showing $\text{Ba } M_{4,5}$ and $\text{La } M_{4,5}$ edges extracted from the regions shown in (a).

elemental identification. The quantification of segregated Ba on the LaInO_3 surface is beyond the scope of this paper. Despite the reduced beam current, the LaInO_3 surface [shown in Figs. 4(a) and 5(a)] becomes partially amorphous due to radiolysis after electron beam irradiation.

A similar analysis was done for a comparable sample grown by PLD to prove that the surface segregation of Ba is independent of the growth method. Here, a 2–3-nm-thin film of LaInO_3 grown on a (001) BaSnO_3 surface was analyzed.

The HAADF-STEM image shown in Fig. 5(a) represents the sample area of the $\text{LaInO}_3/\text{BaSnO}_3$ heterostructure used for the EELS analysis. The EELS signal was collected along the 5 nm interface profile marked by the green arrow,

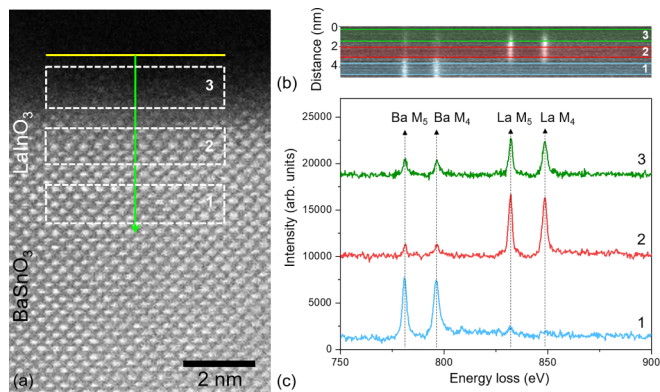


FIG. 5. (a) HAADF STEM image of the $\text{LaInO}_3/\text{BaSnO}_3$ heterostructure grown by PLD showing the area used for the EELS line scan. The green arrow highlights the interface profile of 5 nm length where the EELS signal was collected, while the yellow line indicates the area of lateral integration of the EELS signal. (b) The high-loss EELS line spectrum of the region marked with the green arrow shown in (a). (c) Corresponding EELS spectra of the regions marked with blue (1), red (2), and green (3) shown in (a) and (b).

while the yellow line in Fig. 5(a) shows the lateral integration of the EELS signal. The corresponding high-loss EELS line spectrum is shown in Fig. 5(b) while the integrated EELS spectra from the regions marked with blue, red, and green are extracted in Fig. 5(c). The prominent features are the $\text{Ba } M_{4,5}$ and $\text{La } M_{4,5}$ edges. The $\text{La } M_{4,5}$ edges in the high-loss EELS line spectrum shown in Fig. 5(b) indicate that LaInO_3 growth starts abruptly on the BaSnO_3 surface. However, the signals of the $\text{Ba } M_{4,5}$ edges remain very strong throughout the LaInO_3 film and increase especially on the LaInO_3 surface, indicating the segregation of Ba from BaSnO_3 toward the LaInO_3 surface. This is particularly evident in Fig. 5(c), where the $\text{Ba } M_{4,5}$ edge signal decreases from region 1 toward region 2 and then increases again in region 3. Here, the Ba signal is stronger through the LaInO_3 layer in comparison with the MBE sample, which can be explained by PLD growth kinetics. During PLD growth, the highly accelerated and excited particles bombard the surface with high kinetic energy. This causes Ba atoms to be implanted from the surface into the inner parts of the LaInO_3 film during LaInO_3 film growth, which is not the case with MBE growth.

C. $\text{LaInO}_3/\text{BaSnO}_3$ surface analysis

In addition to the STEM-EELS analysis, $\text{LaInO}_3/\text{BaSnO}_3$ heterostructures with different LaInO_3 layer thicknesses grown by MBE were analyzed by synchrotron-based HAXPES and laboratory-based SXPS. Figure 6 displays the $\text{Ba } 3d_{5/2}$ core level spectra of samples containing 4 and 8 nm LaInO_3 layers collected with varying x-ray photon energy. Energy-dependent spectra have the advantage that the probing depth increases with higher photon energy. In the present case, a threefold increase in probing depth is expected when going from 1.5 to 6.0 keV [34]. By comparison of the Ba spectra, two distinct Ba states can be identified. The lower binding energy (BE) $\text{Ba } 3d_{5/2}$ signal (red curve S2) can be attributed to the Ba signal originating from the main BaSnO_3 layer, while the Ba signal at higher BE (green curve S1) may arise from either the surface or from Ba contamination of the LaInO_3 layer. It should be noted that the observed BE difference of 0.4 eV between the SXPS and HAXPES measurements can be attributed to differences in the measurement setup and possible energy alignment.

To establish whether the detected Ba signal originates from the LaInO_3 surface or is a result of LaInO_3 layer contamination, we model two cases as described in the Supplemental Material [34]. First, we assume that there is 1 monolayer (ML) of BaO present on the surface of the $\text{LaInO}_3/\text{BaSnO}_3$ heterostructure. The ratio of the Ba signal from the BaO surface layer to the Ba signal originating from the BaSnO_3 film was calculated and is illustrated in Fig. 7 for the four different measurements shown in Fig. 6.

In addition to the modeled data, the area ratio of the two Ba contributions in the $\text{Ba } 3d_{5/2}$ experimental spectra taken from peak fit analysis (green and red curves S1 and S2, respectively) is also shown in Fig. 7. When comparing experiment to theory at 1.5 keV, the Ba (BaSnO_3)-to-Ba (BaO) signal ratio is <1 in both the 4 and 8 nm samples. At 3.4 and 6.0 keV, the ratios yield values >1 for both theoretical and experimental values. Therefore, the XPS data and depth distribution

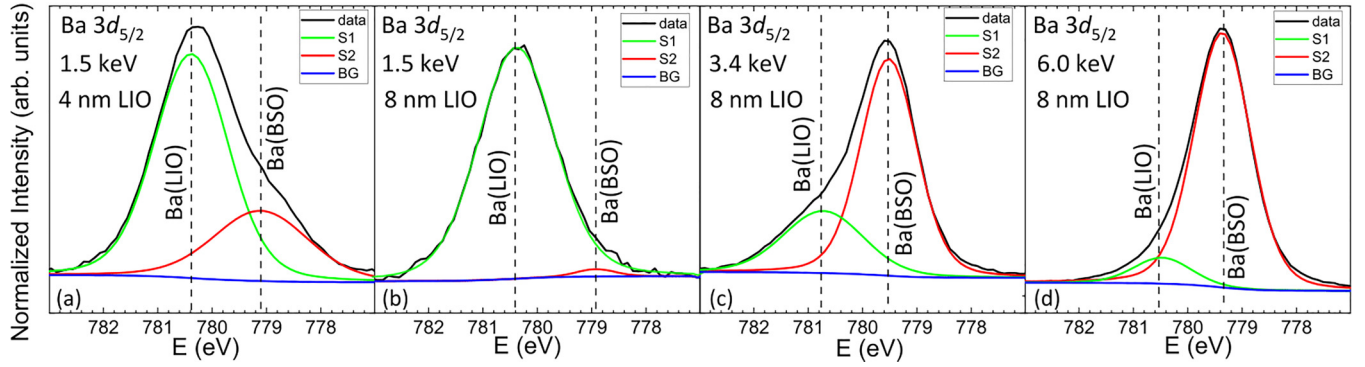


FIG. 6. Ba $3d_{5/2}$ core level spectra of a LaInO₃ (LIO)/BaSnO₃ (BSO) heterostructures at varying photon energies. SXPS data of (a) 4-nm-thick and (b) 8-nm-thick LaInO₃ layer at photon energy of 1.5 keV. HAXPES data of 8-nm-thick LaInO₃ layer at photon energies of (c) 3.4 keV and (d) 6.0 keV. The black lines represent the measured data, while the green and red lines result from peak fitting using the CasaXPS software, assuming two contributions, one from Ba which comes from the BaSnO₃ layer (S2) and one from a Ba signal that either results from a Ba compound inside the LaInO₃ layer or from a Ba surface layer (S1). The blue line represents the Shirley background (BG).

function (DDF) exhibit qualitatively similar characteristics, as would be expected for a single monolayer of BaO on the surface. In the second model, we consider that the Ba signal observed in the spectra may arise due to Ba contamination in the LaInO₃ layer. Our model assumes 10% Ba contamination in the LaInO₃ layer. For the 8-nm-thick LaInO₃ layer, the DDF data match qualitatively with the XPS analysis data. However, for the 4-nm-thick sample, the DDF data indicate a Ba(BaSnO₃)-to-Ba(LaInO₃) signal ratio that is >1 , which contradicts experimental observations. Moreover, to obtain a Ba(BaSnO₃)-to-Ba(LaInO₃) ratio <1 , one would have to assume a Ba contamination of the LaInO₃ layer of at least 27%, which is beyond any experimental observation in these samples. Overall, our findings confirm that the extra feature observed in the Ba $3d_{5/2}$ spectra at a higher BE is due to a Ba surface state rather than LaInO₃ layer contamination, which

is in a good agreement with the STEM-EELS observations for an MBE sample.

Summarizing our experimental results from HRTEM, STEM-EELS, and XPS measurements, we find three main results:

- (i) BaSnO₃ (001) surfaces are BaO terminated. This is true for as-grown epitaxial films as well as for samples annealed in an oxygen atmosphere.
- (ii) Interfaces of BaSnO₃ with LaInO₃ are SnO₂ terminated.
- (iii) Thin films (≤ 8 nm) of LaInO₃ grown on BaSnO₃ show Ba at their as-grown surface, which could be an indication of surface segregation as a mechanism. This finding is independent of the growth method, be it MBE or PLD.

In the following, we will study the thermodynamics of surfaces and interfaces based on DFT.

IV. COMPUTATIONAL RESULTS AND DISCUSSION

A. BaSnO₃ surface

We investigate the surface energies of the BaSnO₃ (001) surface and its terminations. The optimized BaSnO₃ structure with the lattice constant of 4.119 Å is used in the following calculations to construct the slabs and heterostructures. When a stoichiometric BaSnO₃ slab is ideally cleaved, two slabs with complementary surface terminations are created. The cleavage energy is defined as the energy required to separate the crystal into two parts. For example, at the BaSnO₃ (001) surface, BaO/SnO₂ termination can be formed. The surface energy can be estimated as the sum of the cleavage and relaxation energies [36]. The details of the calculations are given in the Supplemental Material [34]. The results of the calculated cleavage, relaxation, and the surface energies for the different terminations of the (001) surface are summarized in Table I.

Comparing the surface energies E_s for the two terminations, we find that BaO has a slightly lower surface energy than SnO₂. Our results are in good agreement with the recently published study by Wang *et al.* [37]. In contrast to our

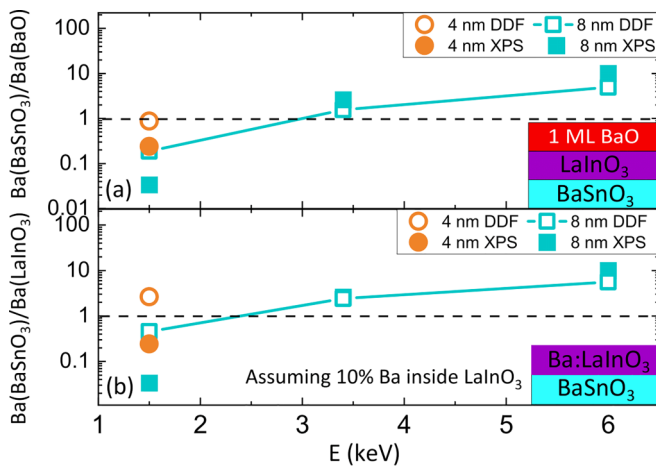


FIG. 7. (a) Ba from BaSnO₃-to-Ba from BaO surface layer ratio derived from XPS analysis (solid icons) and from the DDF model (empty icons) assuming the structure shown in the lower right corner. (b) Ba from BaSnO₃-to-Ba from LaInO₃ contamination ratio derived from XPS analysis (solid icons) and from DDF model (empty icons) assuming the structure in the lower right corner.

TABLE I. Calculated cleavage (E_{cl}), relaxation (E_{rlx}), and surface (E_s) energies for the BaO and SnO₂ terminations of the BaSnO₃ (001) surface.

Surface termination	E_{cl} (J/m ²)	E_{rlx} (J/m ²)	E_s (J/m ²)
BaO	1.162	-0.090	1.072
SnO ₂	1.162	-0.022	1.140

results, Stassi *et al.* [38] reported that the SnO₂ termination is slightly more favorable. This difference can be attributed to the fact that they use a local-density approximation functional, which underestimates the lattice parameters. Looking more closely at the surface relaxation of our optimized slabs, we found that the atomic relaxation occurs mainly in the two top layers, as reported in Ref. [38]. In contrast to their results, we find that the atomic displacements of the BaO-terminated surface layer are higher than for the SnO₂-terminated surface layer (see Fig. S4 in the Supplemental Material [34]). This result is reflected in the values of the relaxation energies. Nevertheless, our result is in excellent agreement with the experimental results from TEM analysis which showed how the BaSnO₃ (001) surface tends to terminate with the BaO layer. To gain more insight into the stability of these two terminations under the specific experimental conditions, we construct the surface stability phase diagram for the BaSnO₃ (001) surface. We compute the surface grand potential as a function of the chemical potentials of the different species, which implies a contact with matter reservoirs. The surface grand potential γ per unit area corresponding to the i termination can be approximated according to [39–42]

$$\gamma(i) = \frac{1}{2A} [E_{slab}(i) - N_{Ba}\mu_{Ba} - N_{Sn}\mu_{Sn} - N_O\mu_O], \quad (1)$$

where A is the surface area, and the factor $\frac{1}{2}$ corresponds to two symmetric surfaces in the slab model. For each termination i , $E_{slab}(i)$ denotes the total energy of the relaxed slab formed by N_{Ba} , N_{Sn} , and N_O of Ba, Sn, and O atoms, respectively, while μ_{Ba} , μ_{Sn} , and μ_O represent their chemical potentials. For the stoichiometric BaSnO₃ phase, the chemical potential μ_{BaSnO_3} is given by the sum of the chemical potentials of all atomic species. Since the surfaces must be in equilibrium with the bulk, the chemical potential μ_{BaSnO_3} is approximated by the total energy of bulk BaSnO₃ [40,42]. Thus, the relation between the chemical potentials can be written as

$$E_{BaSnO_3}^{bulk} \approx \mu_{BaSnO_3} = \mu_{Ba} + \mu_{Sn} + 3\mu_O. \quad (2)$$

The chemical potentials of the different elements are defined as follows:

$$\mu_O = \Delta\mu_O + \frac{E_{O_2}^{mol}}{2}, \quad (3)$$

$$\mu_{Sn} = \Delta\mu_{Sn} + E_{Sn}^{bulk}, \quad (4)$$

$$\mu_{Ba} = \Delta\mu_{Ba} + E_{Ba}^{bulk}, \quad (5)$$

where E_{Ba}^{bulk} , E_{Sn}^{bulk} , and $E_{O_2}^{mol}$ are the total energies of the constituents Ba, Sn, and O in their respective stable bulk reference structures [body-centered cubic (bcc) for Ba and diamondlike

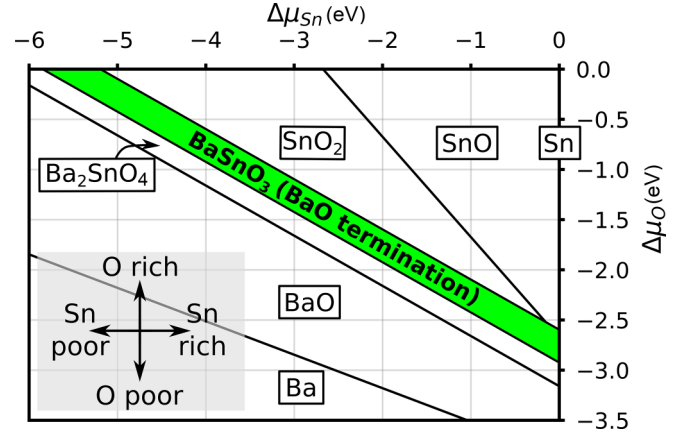


FIG. 8. Surface energy diagram for the BaSnO₃ (001) surface as a function of the chemical potentials of Sn and O, in eV. The BaSnO₃ phase can be formed within the green area, while the favorable termination will be BaO. The boundaries with other precipitates are indicated by the black solid lines.

for Sn], and molecular O₂. To avoid the formation of Ba and Sn precipitations as well as O₂ gas, the chemical potential variation $\Delta\mu$ for each element must be <0 ($\Delta\mu < 0$). Using Eqs. (2)–(5), the surface energy in Eq. (1) can be written as

$$\gamma(i) = \Phi(i) - \frac{1}{2A} [\Delta\mu_{Sn}(N_{Sn} - N_{Ba}) + \Delta\mu_O(N_O - 3N_{Ba})], \quad (6)$$

where $\Phi(i)$ can be expressed as

$$\Phi(i) = \frac{1}{2A} \left[E_{slab}(i) - N_{Ba}E_{BaSnO_3}^{bulk} - (N_{Sn} - N_{Ba})E_{Sn}^{bulk} - (N_O - 3N_{Ba})\frac{E_{O_2}^{mol}}{2} \right]. \quad (7)$$

The range of chemical potential variation $\Delta\mu$ is determined by considering additional thermodynamic limits related to the formation of Ba, BaO, Ba₂SnO₄, SnO₂, SnO, and Sn precipitants (see details in the Supplemental Material) [34].

The calculated surface energy diagram as a function of the independent variables $\Delta\mu_{Sn}$ and $\Delta\mu_O$ for the (001) surface is shown in Fig. 8. Considering the boundaries related to the formation of Ba, BaO, Ba₂SnO₄, SnO₂, SnO, and Sn precipitants, the BaO-terminated BaSnO₃ crystal is found to appear within the narrow area highlighted in green. These results are in a good agreement with previous theoretical studies [43,44]. For a stable BaSnO₃ phase with either BaO or SnO₂ termination, the surface energy $\gamma(i)$ must be positive. However, although both terminations can be energetically stable (since both are positive), the calculated surface energy of BaO is lower than that of SnO₂. Therefore, the BaO termination is energetically more favorable and is more likely to form, while SnO₂ forms as a precipitate.

B. LaInO₃/BaSnO₃ interface

In the following, we will discuss our experimental finding, where despite the energetically favored BaO-terminated free (001) BaSnO₃ surface, we find a SnO₂-terminated interface

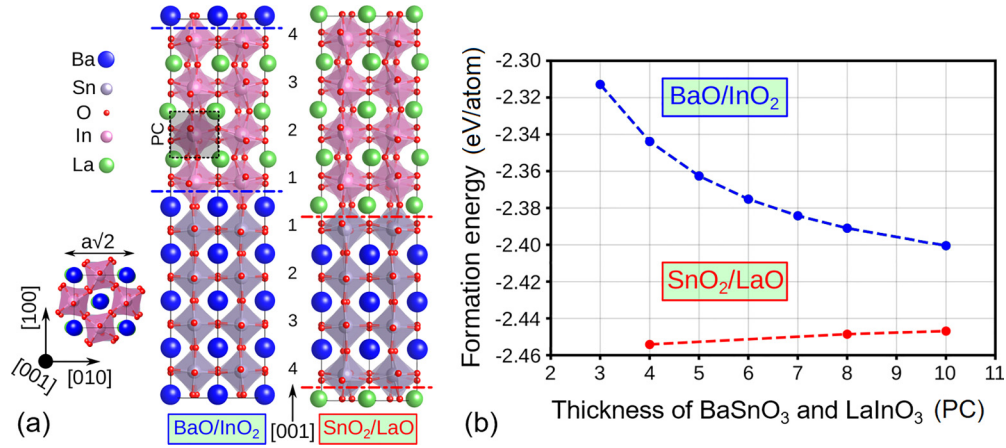


FIG. 9. (a) Top and side views of the symmetric superlattice that is considered to simulate the p - and n -type $\text{LaInO}_3/\text{BaSnO}_3$ interfaces. The in-plane lattice parameter is fixed to that of bulk BaSnO_3 . (b) Variation of the formation energy per atom as a function of the thickness of BaSnO_3 and LaInO_3 layers. PC denotes pseudocubic unit cell as highlighted in (a).

after growing LaInO_3 on BaSnO_3 . We will base our considerations on first-principles calculations. In our previous work, we found that LaInO_3 grows on BaSnO_3 in the form of domains with both (100) and (001) pseudocubic orientations [24]. Both interfaces are degenerate in formation energy. Therefore, to simplify the following DFT calculations, we consider only the $\text{LaInO}_3/\text{BaSnO}_3$ interfaces with (001) pseudocubic orientation of LaInO_3 parallel to the (001) BaSnO_3 surface.

First, we consider the case of four pseudocubic unit cell thick LaInO_3 and compare the formation energies of the different interface terminations. To do this, we adopt the interface models where either LaO/SnO_2 (n -type) or InO_2/BaO (p -type) are periodically replicated (superlattices). In this case, the LaInO_3 block is nonstoichiometric and terminated by a LaO^+ plane (n -type) or InO_2^- (p -type) on both sides [see Fig. 9(a)]. Thus, the system is self-doped and leads to the formation of 2DEG (n -type) or hole gas (p -type) [14]. To minimize the interaction between the periodic interfaces, we converge the values of the formation energies with respect to the thickness of both BaSnO_3 and LaInO_3 sides. We compute their formation energy per atom E_f to rank their relative stability as

$$E_f = \frac{1}{N} \left[E_{\text{tot}}^{\text{interface}} - \sum_{\text{elements}}^N E_{\text{tot}}^{\text{bulk}} \right], \quad (8)$$

where $E_{\text{tot}}^{\text{interface}}$ represents the total energy of the $\text{LaInO}_3/\text{BaSnO}_3$ interface, and $E_{\text{tot}}^{\text{bulk}}$ is the total energy per atom of the constituent elements in their corresponding stable bulk reference structure [face-centered cubic (fcc) for La, bcc for Ba, diamondlike for Sn, and face-centered tetragonal for In], and molecular O_2 . Division by the number of atoms N gives the formation energy in eV per atom.

As shown in Fig. 9(b), the formation energy converges to 0.01 eV/atom for $\text{LaInO}_3/\text{BaSnO}_3$ periodic interfaces. The n -type interface has a formation energy of about -2.45 eV/atom which is 0.05 eV/atom lower than the formation energy of the p -type interface, indicating that the LaO/SnO_2 termination is more favorable to form at the interface.

To validate the segregation of the BaO layer, we consider two nonperiodic interfaces formed by combining stoichiometric LaInO_3 planes on BaO - or SnO_2 -terminated BaSnO_3 substrates (Fig. 10). In the latter termination, we consider the BaO plane on top of the LaInO_3 surface since we expect it to segregate from the interface to the LaInO_3 surface [see Fig. 10(b)].

Looking first at the optimized geometries of the BaO -terminated BaSnO_3 substrate, we find that the formal polarization P_0 is induced in the LaInO_3 side due to charged LaO^+ and InO_2^- planes, oriented from the interface to the surface. Consequently, we find that structural distortions within the LaInO_3 layer induces a polarization ΔP opposite to P_0 to compensate it. Such structural distortions are mainly dominated by oxygen displacement from the bulk positions [14]. Since the LaInO_3 thickness is less than the critical value required for transfer charge to the interface, ΔP is almost the same amount as P_0 (~ 0.47 C/m²) and is fully compensated [14]. Focusing now on the interface with the SnO_2 -terminated surface, we find a similar behavior, but the polarizations are reversed compared with the BaO -terminated interface since the LaInO_3 side starts

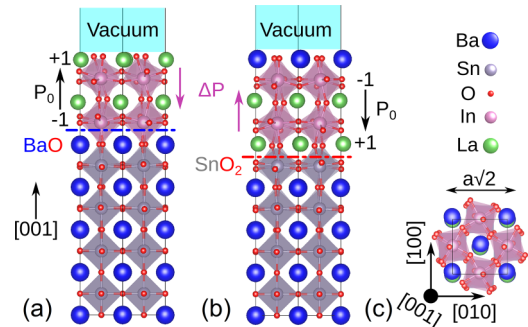


FIG. 10. Side view of the nonperiodic $\text{LaInO}_3/\text{BaSnO}_3$ interface with (a) BaO -terminated and (b) SnO_2 -terminated BaSnO_3 . The orientations of the formal polarization P_0 and polarization induced by structural distortions ΔP are highlighted by black and magenta arrows, respectively, in both panels. The top view of (b) is shown in (c).

from the LaO^{+1} plane. Comparing their total energies, we find that the SnO_2 -terminated interface is more favorable than the BaO-terminated interface by ~ 15 meV/f.u., although it contains a BaO layer on top of LaInO_3 . The obtained results agree with the conclusion that the SnO_2 -terminated interface is more favorable, and they show that the presence of the BaO layer on the LaInO_3 surface makes the interface lower in energy. This outcome is consistent with STEM-EELS and XPS observations of the BaO surface layer.

We refer to our previous work to explain why the n -type interface is energetically more favorable [14]. The 2DEG for the SnO_2 interface forms within the BaSnO_3 side primarily to compensate for the polar discontinuity at the interface. It originates from a charge transfer from the LaInO_3 to the BaSnO_3 side and is accompanied by polar distortions that occur mainly within BaSnO_3 . In the case of the n -type interface, we observe a gradual reduction in the octahedra tilt from the LaInO_3 to the BaSnO_3 side, leading to an expansion of the out-of-plane lattice spacing at the interface. Additionally, this transition results in increased oxygen-cation displacements within BaSnO_3 . This behavior has been experimentally confirmed by Kim *et al.* [45], wherein they observed gradual changes in oxygen octahedral tilt at the interface, accompanied by an increase in lattice spacing. Conversely, for the p -type interface, the oxygen octahedral tilt also gradually diminishes from LaInO_3 to BaSnO_3 . However, in this scenario, the BaO termination promotes the nonpolar distortions in the BaSnO_3 side, confining polar distortions exclusively within the LaInO_3 block. Importantly, the polar distortions limited to the LaInO_3 side contribute less to compensating the interfacial polar discontinuity than the n -type interface, where the polar distortions are primarily localized within the BaSnO_3 region. Consequently, the InO_2/BaO interface is less favorable in terms of formation energy results [14].

V. SUMMARY AND CONCLUSIONS

In this paper, using both TEM experiments and DFT, we clearly demonstrate that the (001) BaSnO_3 surface with BaO termination is energetically favored over a wide range of chemical potentials. In contrast, SnO_2 -terminated surfaces only remain stable under conditions that lead to SnO_2 formation, potentially causing SnO_2 precipitates.

Through our comprehensive analysis of the LaInO_3 and BaSnO_3 heterostructure using STEM-EELS and XPS, we have obtained robust experimental evidence supporting an LaO/SnO_2 interface with pronounced Ba segregation at the growth surface. Our theoretical model further validates this configuration as the most energetically favorable one. Even when a BaO-terminated BaSnO_3 surface is intentionally prepared for epitaxial growth, our results indicate that the $\text{LaInO}_3/\text{BaSnO}_3$ interface will eventually adopt a SnO_2 termination. This segregation of Ba atoms is primarily driven by the need to compensate for the polar discontinuity.

In the case of an n -type SnO_2 -terminated interface, we observe a gradual reduction in the octahedral tilt from LaInO_3 to BaSnO_3 , resulting in an expansion of the out-of-plane lattice spacing at the interface and a polar distortion char-

acterized by increased oxygen-cation displacements within BaSnO_3 . This efficiently compensates for the polar discontinuity. Conversely, the BaO-terminated p -type interface promotes nonpolar distortions within the BaSnO_3 , which effectively confines the polar distortions solely to the LaInO_3 at the interface. This difference in polar discontinuity compensation is the driving factor behind the observed Ba segregation.

While in the case of classical group IV or III–V semiconductors, segregation is primarily driven by minimization of the surface free energy, strain energy, and by solubility, in perovskites, the compensation of the polar discontinuity emerges as a significant driving force [16–19,46–48]. Unlike cubic or hexagonal semiconductors, where the only response to strain is a tetragonal distortion, perovskites offer additional degrees of freedom for adaptation, including octahedral tilts and polar and nonpolar distortions, all of which contribute to minimizing the energy of the system.

ACKNOWLEDGMENTS

This paper was supported by the Leibniz Senatsausschuss Wettbewerb project BaStet (Grant No. K74/2017) and was performed in the framework of GraFOx, a Leibniz science campus partially funded by the Leibniz Association. The research leading to partial EELS results has received funding from the European Union’s Horizon 2020 research and innovation program under Grant Agreement No. 823717-ESTEEM3. We acknowledge the North-German Supercomputing Alliance for providing high-performance computing resources that have contributed to the research results reported in this paper (Project No. bep00078). F.P.S. and T.L. acknowledge the German Federal Ministry for Education and Research (BMBF) under the grant CatLab (Grant No. 03EW0015B) for funding. A.A.R. acknowledges support from the Department of Chemistry, UCL. A.R. acknowledges support from the Analytical Chemistry Trust Fund for her CAMS-UK Fellowship. A.R. acknowledges support from the Institute of Physics carer’s fund, which provided financial support to enable her to attend the HAXPES experiments at PETRAIII in person. The authors also acknowledge DESY (Hamburg, Germany), a member of the Helmholtz Association, for the provision of experimental facilities. Parts of this paper were carried out at PETRAIII using beamline P22. Beamtime was allocated for Proposal No. I-20221263. Funding for the HAXPES instrument by the BMBF under framework program ErUM is gratefully acknowledged. The authors acknowledge Prof. Dr. Kookrin Char (Seoul National University) for providing the PLD-grown samples and for valuable discussions. We also thank Dr. Toni Markurt (Leibniz-Institut für Kristallzüchtung) for fruitful discussions in the early stages of this work. We thank Thilo Remmele (Leibniz-Institut für Kristallzüchtung) for TEM technical support, Dr. Aykut Baki (Leibniz-Institut für Kristallzüchtung) for sample annealing, and Albert Kwasniewski (Leibniz-Institut für Kristallzüchtung) for the x-ray crystallographic orientation of the BaSnO_3 single crystals.

- [1] G. A. Baraff, J. A. Appelbaum, and D. R. Hamann, Self-consistent calculation of the electronic structure at an abrupt GaAs-Ge interface, *Phys. Rev. Lett.* **38**, 237 (1977).
- [2] W. E. Pickett, S. G. Louie, and M. L. Cohen, Ge-GaAs (110) interface: A self-consistent calculation of interface states and electronic structure, *Phys. Rev. Lett.* **39**, 109 (1977).
- [3] I. P. Smorchkova, L. Chen, T. Mates, L. Shen, S. Heikman, B. Moran, S. Keller, S. P. DenBaars, J. S. Speck, and U. K. Mishra, AlN/GaN and (Al, Ga) N/AlN/GaN two-dimensional electron gas structures grown by plasma-assisted molecular-beam epitaxy, *J. Appl. Phys.* **90**, 5196 (2001).
- [4] A. Ohtomo and H. Y. Hwang, A high-mobility electron gas at the LaAlO₃/SrTiO₃ heterointerface, *Nature (London)* **427**, 423 (2004).
- [5] N. Nakagawa, H. Y. Hwang, and D. A. Muller, Why some interfaces cannot be sharp, *Nat. Mater.* **5**, 204 (2006).
- [6] G. Herranz, G. Singh, N. Bergeal, A. Jouan, J. Lesueur, J. Gázquez, M. Varela, M. Scigaj, N. Dix, F. Sánchez *et al.*, Engineering two-dimensional superconductivity and Rashba spin-orbit coupling in LaAlO₃/SrTiO₃ quantum wells by selective orbital occupancy, *Nat. Commun.* **6**, 6028 (2015).
- [7] S. Nazir, M. Behtash, and K. Yang, Towards enhancing two-dimensional electron gas quantum confinement effects in perovskite oxide heterostructures, *J. Appl. Phys.* **117**, 115305 (2015).
- [8] A. Janotti, L. Bjaalie, L. Gordon, and C. G. Van de Walle, Controlling the density of the two-dimensional electron gas at the SrTiO₃/LaAlO₃ interface, *Phys. Rev. B* **86**, 241108 (2012).
- [9] D.-W. Kim, D.-H. Kim, B.-S. Kang, T. W. Noh, D. R. Lee, and K.-B. Lee, Roles of the first atomic layers in growth of SrTiO₃ films on LaAlO₃ substrates, *Appl. Phys. Lett.* **74**, 2176 (1999).
- [10] C. Noguera, *Physics and Chemistry at Oxide Surfaces* (Cambridge University Press, Cambridge, 1996).
- [11] S. A. Chambers, M. H. Engelhard, V. Shutthanandan, Z. Zhu, T. C. Droubay, L. Qiao, P. V. Sushko, T. Feng, H. D. Lee, T. Gustafsson *et al.*, Instability, intermixing and electronic structure at the epitaxial LaAlO₃/SrTiO₃ (001) heterojunction, *Surf. Sci. Rep.* **65**, 317 (2010).
- [12] H. J. Kim, U. Kim, Kim, T. H. Kim, H. S. Mun, B.-G. Jeon, K. T. Hong, W.-J. Lee, C. Ju, K. H. Kim *et al.*, High mobility in a stable transparent perovskite oxide, *Appl. Phys. Express* **5**, 061102 (2012).
- [13] U. Kim, C. Park, Y. M. Kim, J. Shin, and K. Char, Conducting interface states at LaInO₃/BaSnO₃ polar interface controlled by Fermi level, *APL Mater.* **4**, 071102 (2016).
- [14] W. Aggoune and C. Draxl, Tuning two-dimensional electron and hole gases at LaInO₃/BaSnO₃ interfaces by polar distortions, termination, and thickness, *npj Comput. Mater.* **7**, 174 (2021).
- [15] Y. Kim, Y. M. Kim, J. Shin, and K. Char, LaInO₃/BaSnO₃ polar interface on MgO substrates, *APL Mater.* **6**, 096104 (2018).
- [16] J. F. Nützel and G. Abstreiter, Segregation and diffusion on semiconductor surfaces, *Phys. Rev. B* **53**, 13551 (1996).
- [17] O. Dehaese, X. Wallart, and F. Molloy, Kinetic model of element III segregation during molecular beam epitaxy of III-III'-V semiconductor compounds, *Appl. Phys. Lett.* **66**, 52 (1995).
- [18] S. Froyen and A. Zunger, Surface segregation and ordering in III-V semiconductor alloys, *Phys. Rev. B* **53**, 4570 (1996).
- [19] P. Bogusławski, K. Rapcewicz, and J. J. Bernholc, Surface segregation and interface stability of AlN/GaN, GaN/InN, and AlN/InN {0001} epitaxial systems, *Phys. Rev. B* **61**, 10820 (2000).
- [20] T. Maekawa, K. Kurosaki, and S. Yamanaka, Thermal and mechanical properties of polycrystalline BaSnO₃, *J. Alloys Compd.* **416**, 214 (2006).
- [21] H. M. Park, H. J. Lee, S. H. Park, and H. I. Yoo, Lanthanum indium oxide from x-ray powder diffraction, *Acta Cryst. C* **59**, i131 (2003).
- [22] Z. Galazka, K. Irmscher, S. Ganschow, M. Zupancic, W. Aggoune, C. Draxl, M. Albrecht, D. Klimm, A. Kwasniewski, T. Schulz *et al.*, Melt growth and physical properties of bulk LaInO₃ single crystals, *Physica Status Solidi (a)* **218**, 2100016 (2021).
- [23] A. M. Glazer, The classification of tilted octahedra in perovskites, *Acta Cryst. B* **28**, 3384 (1972).
- [24] M. Zupancic, W. Aggoune, T. Markurt, Y. Kim, Y. M. Kim, K. Char, C. Draxl, and M. Albrecht, Role of the interface in controlling the epitaxial relationship between orthorhombic LaInO₃ and cubic BaSnO₃, *Phys. Rev. Mater.* **4**, 123605 (2020).
- [25] Z. Galazka, R. Uecker, K. Irmscher, D. Klimm, R. Bertram, A. Kwasniewski, M. Naumann, R. Schewski, M. Pietsch, U. Juda *et al.*, Melt growth and properties of bulk BaSnO₃ single crystals, *J. Phys.: Condens. Matter* **29**, 075701 (2016).
- [26] R. Dirsyte, J. Schwarzkopf, G. Wagner, R. Fornari, J. Lienemann, M. Busch, and H. Winter, Thermal-induced change in surface termination of DyScO₃ (110), *Surf. Sci.* **604**, L55 (2010).
- [27] G. Hoffmann, M. Budde, P. Mazzolini, and O. Bierwagen, Efficient suboxide sources in oxide molecular beam epitaxy using mixed metal+ oxide charges: The examples of SnO and Ga₂O, *APL Mater.* **8**, 031110 (2020).
- [28] G. Hoffmann *et al.*, Adsorption-controlled plasma-assisted molecular beam epitaxy of LaInO₃ on DyScO₃ (110): Growth window, strain relaxation, and domain pattern, *Phys. Rev. Mater.* **7**, 084605 (2023).
- [29] C. Schlueter, A. Gloskovskii, K. Ederer, I. Schostak, S. Piec, I. Sarkar, Yu. Matveyev, P. Lömker, M. Sing, R. Claessen *et al.*, The new dedicated HAXPES beamline P22 at PETRAIII, *AIP Conf. Proc.* **2054**, 040010 (2019).
- [30] P. Hohenberg and W. J. P. R. Kohn, Density functional theory (DFT), *Phys. Rev* **136**, B864 (1964).
- [31] W. Kohn and L. J. Sham, Self-consistent equations including exchange and correlation effects, *Phys. Rev.* **140**, A1133 (1965).
- [32] J. P. Perdew, A. Ruzsinszky, G. I. Csonka, O. A. Vydrov, G. E. Scuseria, L. A. Constantin, X. Zhou, and K. Burke, Restoring the density-gradient expansion for exchange in solids and surfaces, *Phys. Rev. Lett.* **100**, 136406 (2008).
- [33] V. Blum, R. Gehrke, F. Hanke, P. Havu, V. Havu, X. Ren, K. Reuter, and M. Scheffler, *Ab initio* molecular simulations with numeric atom-centered orbitals, *Comput. Phys. Commun.* **180**, 2175 (2009).
- [34] See Supplemental Material at <http://link.aps.org/supplemental/10.1103/PhysRevMaterials.8.034602> for more details on EELS and XPS analysis, and DFT calculations.
- [35] K. Momma and F. Izumi, VESTA 3 for three-dimensional visualization of crystal, volumetric and morphology data, *J. Appl. Cryst.* **44**, 1272 (2011).

- [36] R. I. Eglitis and D. Vanderbilt, *Ab initio* calculations of BaTiO₃ and PbTiO₃ (001) and (011) surface structures, *Phys. Rev. B* **76**, 155439 (2007).
- [37] Y. Wang, Z. Zhang, Y. Wang, E. Doan, L. Yuan, W. Tang, and K. Yang, First-principles investigation of structural, electronic, and energetic properties of BaSnO₃ (001) surfaces, *Vacuum* **212**, 111977 (2023).
- [38] A. Slassi, M. Hammi, and O. El Rhazouani, Surface relaxations, surface energies and electronic structures of BaSnO₃ (001) surfaces: *Ab initio* calculations., *J. Electron. Mater.* **46**, 4133 (2017).
- [39] F. Bottin, F. Finocchi, and C. Noguera, Stability and electronic structure of the (1 × 1) SrTiO₃ (110) polar surfaces by first-principles calculations, *Phys. Rev. B* **68**, 035418 (2003).
- [40] Yu. A. Mastrikov, E. Heifets, E. A. Kotomin, and J. Maier, Atomic, electronic and thermodynamic properties of cubic and orthorhombic LaMnO₃ surfaces, *Surf. Sci.* **603**, 326 (2009).
- [41] E. Heifets, E. A. Kotomin, Y. A. Mastrikov, S. Piskunov, and J. Maier, in *Thermodynamics*, edited by J. C. Moreno-Pirajan (IntechOpen, Rijeka, 2011), Chap. 19.
- [42] Y. Wang, J. Cheng, M. Behtash, W. Tang, J. Luob, and K. Yang, First-principles studies of polar perovskite KTaO₃ surfaces: Structural reconstruction, charge compensation, and stability diagram, *Phys. Chem. Chem. Phys.* **20**, 18515 (2018).
- [43] D. O. Scanlon, Defect engineering of BaSnO₃ for high-performance transparent conducting oxide applications, *Phys. Rev. B* **87**, 161201 (2013).
- [44] S. Dabaghmanesh, R. Saniz, M. N. Amini, D. Lamoen, and B. Partoens, Perovskite transparent conducting oxides: An *ab initio* study, *J. Phys.: Condens. Matter* **25**, 415503 (2013).
- [45] Y. M. Kim, T. Markurt, Y. Kim, M. Zupancic, J. Shin, M. Albrecht, and K. Char, Interface polarization model for a 2-dimensional electron gas at the BaSnO₃/LaInO₃ interface, *Sci. Rep.* **9**, 16202 (2019).
- [46] C. Guille, F. Houzay, J. M. Moison, and F. Barthe, Intermixing at InAs/GaAs and GaAs/InAs interfaces, *Surf. Sci.* **189**, 1041 (1987).
- [47] J. M. Moison, C. Guille, F. Houzay, F. Barthe, and M. Van Rompay, Surface segregation of third-column atoms in group III-V arsenide compounds: Ternary alloys and heterostructures, *Phys. Rev. B* **40**, 6149 (1989).
- [48] F. Turco and J. Massies, Quantitative evaluation of the surface segregation in III-V ternary alloys by x-ray photoelectron spectroscopy, *Appl. Surf. Sci.* **37**, 160 (1989).